nature energy

Article

https://doi.org/10.1038/s41560-025-01885-8

# Improved damp heat and thermal cycling stability of organic solar cells

Received: 14 March 2025

Accepted: 17 September 2025

**Jian Qin[1,2], Qian Xi[1,2], Na Wu[2], Bowen Liu[2,3], Chao Yue[4], Jin Fang[2,5], Zhenguo Wang[2], Yanbin Du[6], Qing Zhang[7], Zhen Wang[1,2], Wei Wang[2], Muhammad Jawad[1,2], Jinjing Qiu[2], Weishi Li[4], Qun Luo[1,2] & Chang-Qi Ma[1,2]**

Despite significant advancements in power conversion efficiency, thermal instability remains a key challenge for organic photovoltaics. Here we propose a stabilization strategy that addresses both intrinsic and extrinsic stability. We first introduce the UV–vis absorption onset temperature ($T_{\mathrm{onset}}$) as a metric for evaluating the intrinsic thermal stability of polymer blends, enabling material screening. Then, we identify interfacial chemical reactions at the polymer blend/$MoO_3$ interface as the primary extrinsic thermal degradation pathway, which can be suppressed by inserting a thin $C_{60}$ interlayer that consequently improves thermal stability of the cells. Finally, by establishing quantitative models to characterize the moisture diffusion over the encapsulated cells, we can quantify the effectiveness of encapsulation. These advances enable organic photovoltaic cells with approximately 18% efficiency to retain 94% of their initial efficiency after 1,032-hour 85 °C/85% relative humidity damp heat and 200 thermal cycles (−40 °C to 85 °C) tests, among the highest stabilities reported under the damp heat (ISOS-D-3) and thermal cycling (ISOS-T-3) testing standards.

Organic photovoltaics (OPVs) are gaining traction as a promising solar technology in the global energy transition due to their advantages, such as light weight, flexibility and potential for low-cost solution-based manufacturing. These properties enable broad applications, including in near space[1–3], agrivoltaics[4,5], building-integrated photovoltaics[6] and the Internet of Things[7,8] and so on. Advances in organic semiconductor materials and the optimization of bulk heterojunction thin-film morphology have enabled OPVs to achieve over 20% power conversion efficiency (PCE) under standard AM1.5 G conditions[9–11] and more than 30% in controlled indoor low light[12,13], underscoring their real-world potential. Despite recent efficiency achievements, OPVs still fall short of the long-term stability of silicon- and compound-semiconductor-based photovoltaics (Fig. 1b and Supplementary Table 1). Breakthroughs in elucidating photo-degradation mechanisms[14–16], developing interface stabilization using fullerene derivatives[17,18] and Lewis acids[19,20] and doping with a third component[21,22] have significantly extended OPV lifetimes. Specifically, Li et al. demonstrated a long operating lifetime of over 30 years[18,23]. However, instability under damp heat and thermal cycling remains a critical bottleneck for commercialization. For the damp heat and thermal cycling, International Summit on Organic and Hybrid Photovoltaics Stability (ISOS) protocols provide standardized test methods, serving as the basis for evaluating reliability,

---

[1]School of Nano-Tech and Nano-Bionics, University of Science and Technology of China, Hefei, People's Republic of China. [2]i-Lab & Printable Electronics Research Center, Suzhou Institute of Nano-Tech and Nano-Bionics, Chinese Academy of Sciences, SEID, SIP, Suzhou, People's Republic of China. [3]College of Chemistry and Molecular Sciences, Henan University, Kaifeng, People's Republic of China. [4]Key Laboratory of Fluorine and Nitrogen Chemistry and Advanced Materials, Shanghai Institute of Organic Chemistry, Chinese Academy of Sciences, Shanghai, People's Republic of China. [5]Hyper PV Technology Co. Ltd., Jiaxing, China. [6]Anhui Yangde Temperature Control Technology Co., Ltd, Lu'an, People's Republic of China. [7]Vacuum Interconnected Nanotech Workstation (Nano-X), Suzhou Institute of Nano-Tech and Nano-Bionics, Chinese Academy of Sciences, Suzhou, People's Republic of China. e-mail: qluo2011@sinano.ac.cn; cqma2011@sinano.ac.cn

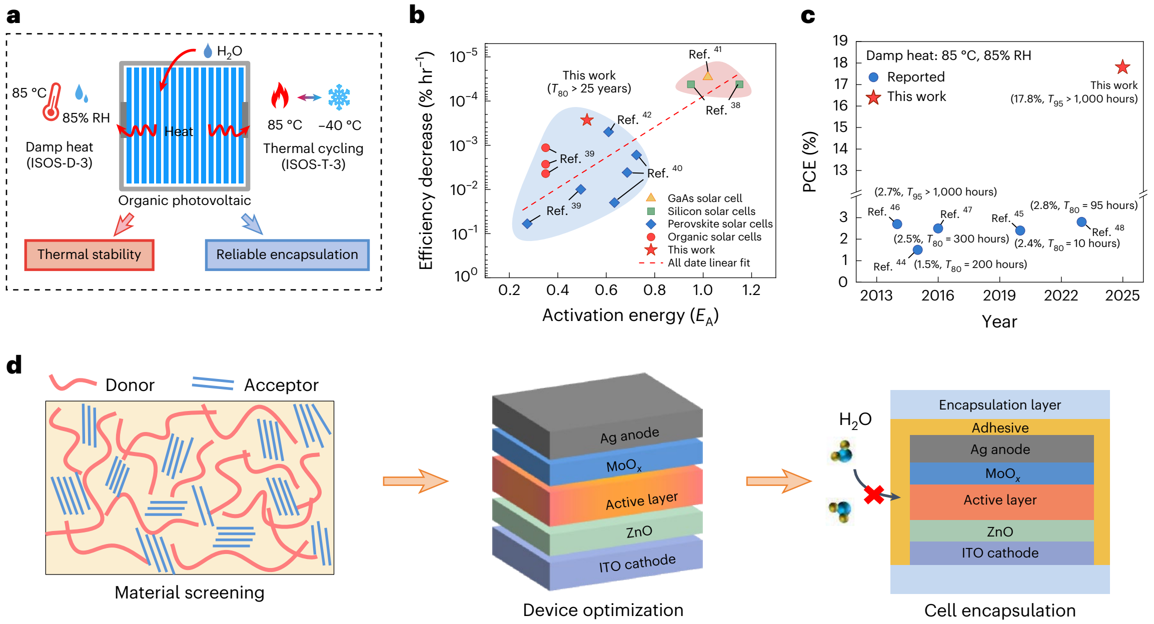

**Fig. 1 | Strategic framework for highly stable OPVs. a**, ISOS-standard accelerated stability tests for OPVs: damp heat (ISOS-D-3) and thermal cycling (ISOS-T-3) protocols. **b**, Comparative analysis of activation energies and operational lifetimes across solar cell technologies (approximate benchmarking highlighting stability gaps)[48–53]. $E_A$ represents the activation energy for degradation of the cells at the anticipated operating temperature. Blue and pink shading is used to distinguish emerging photovoltaics from those already commercialized. **c**, Reported damp heat stability performance (85 °C, 85% RH) for OPVs in literature[54–58]. $T_{80}$ and $T_{95}$ represent the time to 80% and 95% initial efficiency, respectively. A *y*-axis break is applied for visual clarity. **d**, Schematic diagram of the three steps to achieve stable OPVs.

thereby demonstrating the reliability on the ISOS protocols is essential. According to ISOS protocols[24], OPV products must undergo harsh environmental tests, including damp heat (ISOS-D-3) and thermal cycling tests (ISOS-T-3) (Fig. 1a), to evaluate their long-term reliability. However, few studies have reported the reliability of high-efficiency polymer:non-fullerene OPVs under ISOS-D-3 and ISOS-T-3 conditions, with existing research primarily focusing on P3HT:$PC_{61}BM$ cells (Fig. 1c and Supplementary Table 2), highlighting a critical gap in the field.

Enhancing the damp heat and thermal cycling stability of OPVs demands a comprehensive strategy that concurrently optimizes the active layer morphology, device structural robustness and effective encapsulation (Fig. 1d). In a molecular level, given that organic molecules typically exhibit high thermal diffusion coefficients, elevated temperatures induce significant molecular mobility, resulting in morphological changes that can compromise both efficiency and stability[25–28]. More importantly, it is critical to develop reliable methods to evaluate the thermal stability of the organic active layer, enabling the screening of donor:acceptor combinations with superior thermal resilience. At the device level, thermal-induced unexpected interfacial chemical reactions[29,30], molecular interdiffusions[31,32] and mismatches in thermal expansion coefficients of different layers[33,34] can lead to interface degradation and consequently lower the device reliability. Therefore, a thorough understanding of the thermal degradation mechanisms at these interfaces and targeted optimization of the interfacial properties are essential for improving the inherent thermal stability of OPVs. Ultimately, implementing durable encapsulation strategies that protect the device from reactive water and oxygen is essential for sustaining long-term device performance[35–37]. Organic photovoltaics can only withstand damp heat and thermal cycling tests when three criteria are simultaneously achieved: morphologically stable photoactive layers, thermodynamically robust interfaces and hermetically sealed encapsulation architectures.

In this study, temperature-dependent UV–vis absorption measurements identified the onset temperature ($T_{onset}$) of a polymer blend as a critical threshold for molecular mobility activation, establishing it as a quantitative metric for the thermal stability of semiconducting polymer blends. With this critical $T_{onset}$, we quantitatively analysed the intrinsic thermal stability of different polymer blends and consequently screened candidates for OPVs. Additionally, by investigating thermally induced organic active layer/$MoO_3$ interfacial degradation in inverted OPVs, we demonstrated that inserting a thin $C_{60}$ interlayer between the active layer and $MoO_3$ mitigates the ‘burn-in’ degradation, ensuring high intrinsic thermal stability. Furthermore, we introduced a hot-press encapsulation method of using aluminium foil butyl tape (ABT), which exhibits a low lateral water vapour diffusion rate, effectively preventing moisture ingress. As a result, OPVs with an initial PCE of ~18% retained 94% efficiency after 1,032 hours of damp heat (85 °C, 85% relative humidity (RH)) and 200 thermal cycles (−40 °C to 85 °C) tests, demonstrating the most stable, high-efficiency inverted OPVs under the ISOS-D-3 and ISOS-T-3 standards.

## Screening the thermal stability of polymer:non-fullerene blend films

Because nanoscale donor–acceptor separation critically affects the device performance, it is essential to develop a robust methodology for analysing the thermal stability of the active layer, which can facilitate effective material screening[21]. Samuel et al. developed a method to characterize the glass transition temperature ($T_g$) of organic thin films based on the changes in the UV–vis absorption spectroscopy of the films upon different thermal annealing temperatures[38]. Following this, L8-BO film (Supplementary Fig. 1 provides the molecular structure) was tested, and the deviation metric in UV–vis absorption as a function of annealing temperature is shown in Fig. 2a. A high $T_g$ of 113 °C was deduced according to Samuel’s protocol (Supplementary Note 1). Notably, a significant deviation metric of the ultraviolet–visible spectrum is found even at temperatures far below 113 °C (the red triangle), suggesting that molecular thermal motion began before reaching the measured $T_g$. This phenomenon is consistent across various polymers, non-fullerene acceptors and blend films (Supplementary Figs. 2–10).

To determine the temperature at which the film begins to change, we first fit the data to a smooth curve and then differentiate the deviation

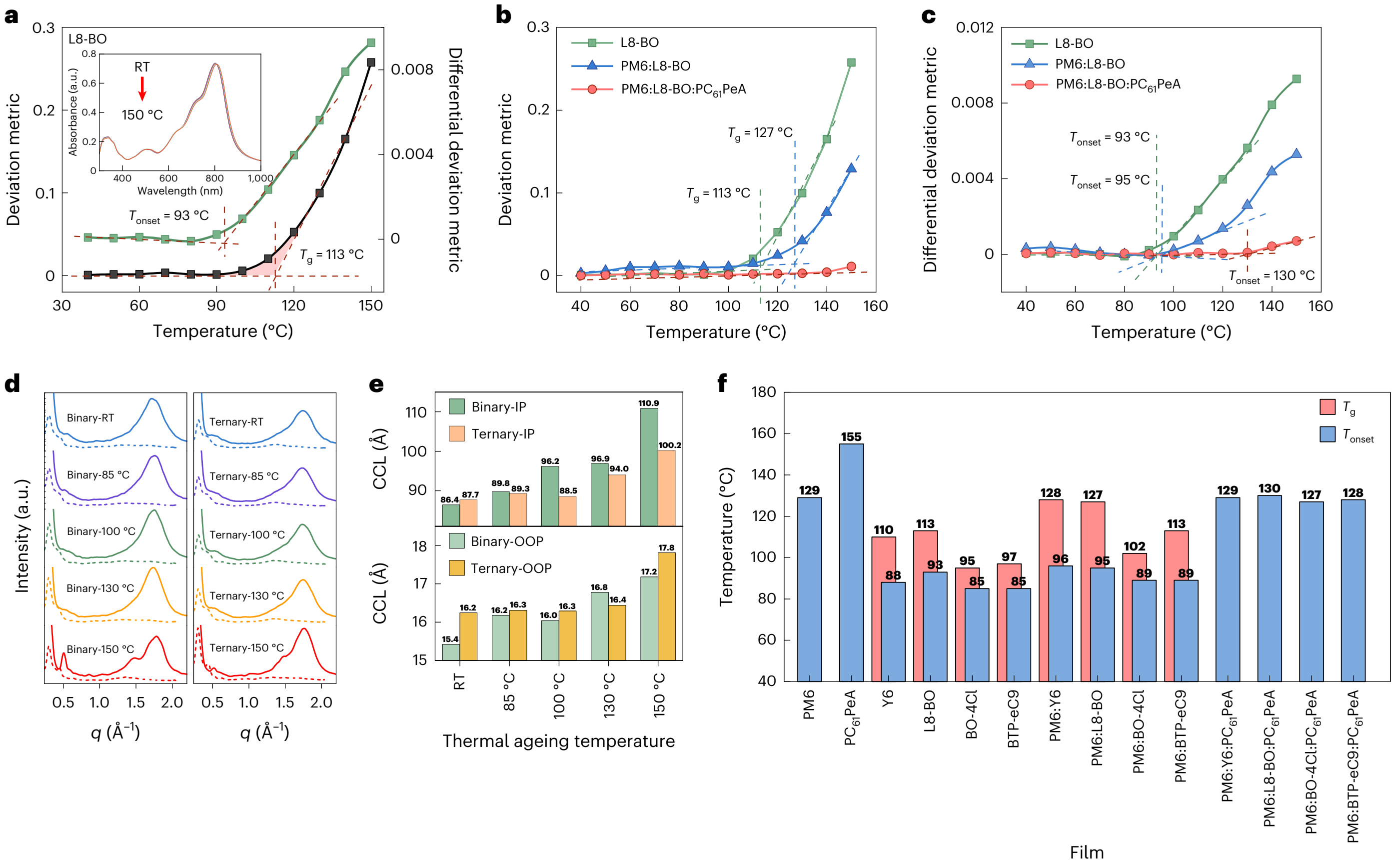

**Fig. 2 | Quantitative analysis of thermal stability in polymer blends for OPVs.** **a**, UV–vis absorption deviation metric and its differential plots as a function of annealing temperature for L8-BO thin films. The curves are obtained by segmented linear fitting, determining $T_g$ = 113 °C and $T_{onset}$ = 93 °C. The inset shows the UV–vis absorption spectra of the films at different temperatures. **b**, The deviation metric of L8-BO, PM6:L8-BO and PM6:L8-BO:PC$_{61}$PeA films at different temperatures. The curves are obtained by segmented linear fitting. **c**, The differential deviation metric of L8-BO, PM6:L8-BO and PM6:L8-BO:PC$_{61}$PeA films from room temperature at different temperatures. The curves are obtained by segmented linear fitting. **d**, 1D scattering profiles of PM6:L8-BO- and PM6:L8-BO:PC$_{61}$PeA-blend films before and after 1,000 hours of annealing at different temperatures (dashed lines, IP; solid lines, OOP). RT represents room temperature. **e**, Crystalline coherence length (CCL) comparison between binary and ternary films before and after prolonged annealing. **f**, Summary of $T_g$ and $T_{onset}$ for single-component, binary and ternary-blend films comprising the polymer donor PM6, various non-fullerene acceptors and the third component PC$_{61}$PeA. The $T_g$ of PM6, PC$_{61}$PeA and ternary blends remained undetectable due to the absence of a clear inflection in the UV–vis absorption deviation metric within the tested temperature range. Chemical structures of these materials are provided in Supplementary Fig. 1.

metric with respect to temperature. Figure 2a presents the results for the L8-BO sample, where the onset of absorption deviation metric, defined as $T_{onset}$, serves as a quantitative indicator of molecular motion in the blend films. For L8-BO, $T_{onset}$ is estimated at 93 °C, significantly lower than its measured $T_g$. Applying this method to a binary blend of L8-BO and PM6 (Fig. 2b,c), we determined a $T_g$ of 127 °C and a $T_{onset}$ of 95 °C, respectively. Both values are higher than those of pristine L8-BO, indicating that the polymer donor matrix restricts the thermal motion of non-fullerene acceptors molecules. Our earlier screening of fullerene-based materials indicated that the cross-linkable PC$_{61}$PeA can enhance OPV efficiency (Supplementary Table 7 and Supplementary Fig. 11). UV–vis spectroscopy of the PC$_{61}$PeA-blended PM6:L8-BO film revealed a $T_{onset}$ of 130 °C, significantly higher than that of the binary blend, suggesting that PC$_{61}$PeA further suppresses molecular motion. Because UV–vis spectra are sensitive to π–π interactions, the $T_g$ reflects major changes in backbone stacking, while $T_{onset}$ captures subtle molecular motion initiated by flexible side chains. These small-scale motions can induce substantial long-term reorganization of π–π stacks, making $T_{onset}$ an ideal indicator of intrinsic thermal stability in polymer blends. To verify this, we tracked morphological evolution in PM6:L8-BO and PM6:L8-BO:PC$_{61}$PeA films under long-term annealing using grazing-incidence wide-angle X-ray scattering (GIWAXS) (Supplementary Fig. 12). The one-dimensional (1D) profiles and CCL analysis (Fig. 2d,e) show that the binary film exhibits increased in-plane (IP) crystallinity after annealing at 100 °C (above $T_{onset}$ = 95 °C), whereas out-of-plane (OOP) changes occur only above $T_g$ (127 °C). Similarly, the ternary blend shows IP changes at 130 °C and OOP changes at 150 °C. Given that IP crystallization strongly affects the active layer/electrode interface and device performance, we propose $T_{onset}$ as a more relevant parameter than $T_g$ for evaluating intrinsic thermal stability in device applications.

Finally, we assessed the $T_g$ and $T_{onset}$ of single-component, binary- and ternary-blend films using PM6 as the donor and L8-BO, Y6, BO-4Cl and BTP-eC9 as acceptors, with PC$_{61}$PeA incorporated as the third component in ternary blends (raw data in Supplementary Figs. 2–10 and Supplementary Table 4), as shown in Fig. 2f. The $T_{onset}$ values for all four binary blends exceeded 85 °C, indicating sufficient stability under standard testing conditions (85 °C limit). The addition of PC$_{61}$PeA combined with high-temperature annealing significantly enhanced the $T_{onset}$ of the blend films, with ternary films reaching values close to 130 °C, demonstrating excellent thermal stability.

## Thermal-driven interfacial degradation and stability enhancement via molecular protection layers

The most widely investigated PM6:L8-BO blend with a $T_{onset}$ higher than 85 °C was chosen as the bulk heterojunction layer to study the degradation behaviour of the cells at a device level. Unencapsulated

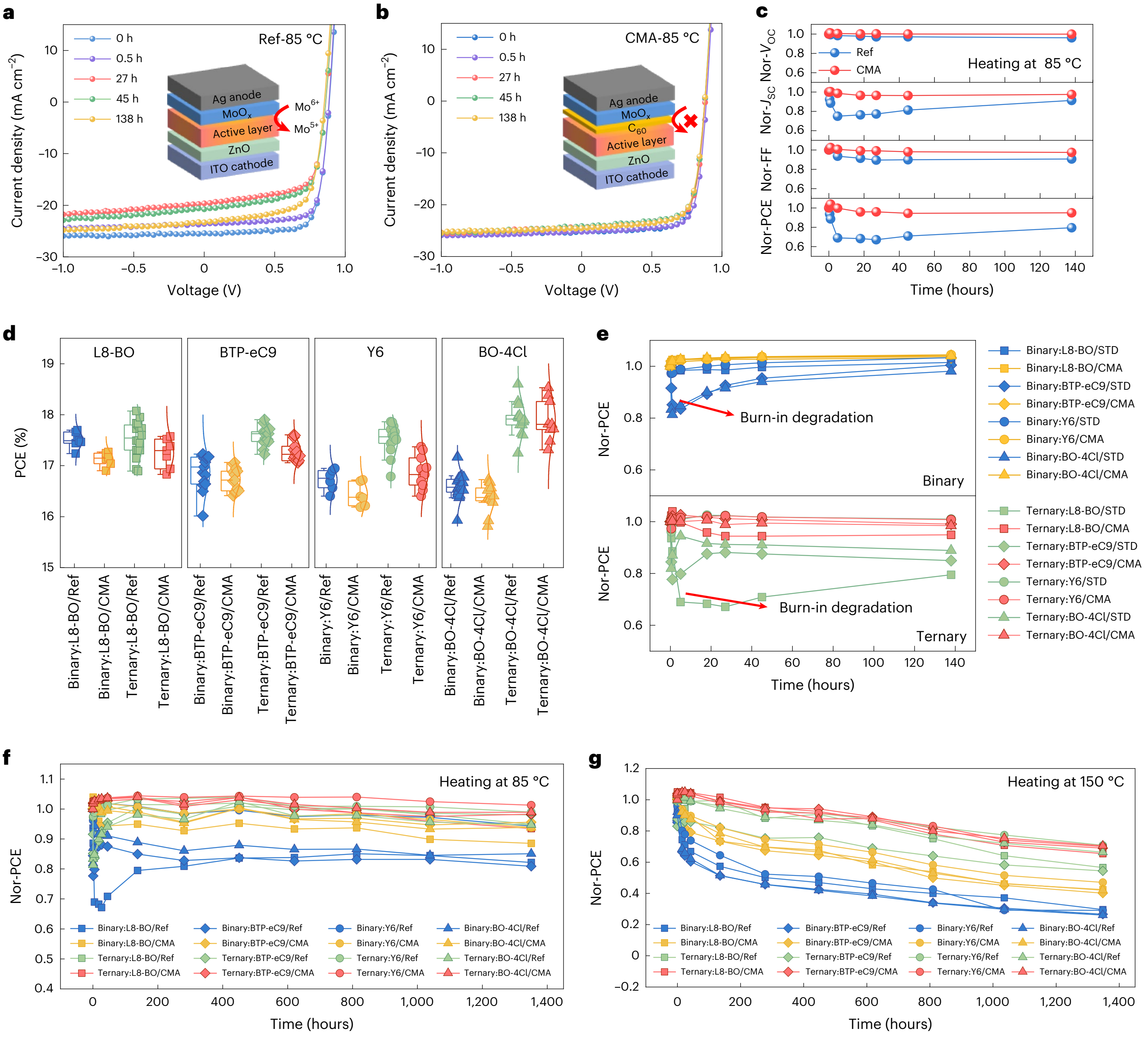

**Fig. 3 | Thermal-induced performance degradation and suppression method by interface protection.** **a**,**b**, Representative *J*–*V* curves of the reference (the Ref-cell; **a**) and $C_{60}$-protected (the CMA-cell; **b**) inverted PM6:L8-BO cells annealed at 85 °C. The insets are the structural schematic diagram of the Ref-cell and the CMA-cell. **c**, Photovoltaic performance evolution of the reference and $C_{60}$-protected PM6:L8-BO cells annealed at 85 °C for 138 hours. The initial PCEs for the Ref-cell and CMA-cell were 16.85% and 16.90%, respectively. **d**, PCE of binary and ternary cells with (CMA) or without (Ref) $C_{60}$ protection layer. The box plots show the minimum, maximum, median and first and third quartiles. Specifically, the centre line represents the median (50th percentile); the bounds of the box indicate the first (25th percentile) and third (75th percentile) quartiles; the whiskers extend to the minimum and maximum values. The statistical results are based on at least six individual devices. **e**, PCE evolution of the various binary (top) and ternary (bottom) cells with (CMA) or without (Ref) $C_{60}$ protection layer annealed at 85 °C. **f**,**g**, PCE evolution of various binary and ternary cells with (CMA) or without (Ref) $C_{60}$ protection layer upon long-term heating at 85 °C (**f**) and 150 °C (**g**). The binary cells were cells with PM6 as the donor and L8-BO, BTP-eC9, Y6 and BO-4Cl as acceptors, respectively. The ternary cells were cells with $PC_{61}PeA$ doped as the third component. Photovoltaic parameters are included in the source data file.

devices with a structure of indium tin oxide (ITO)/ZnO/PM6:L8-BO/$MoO_3$/Ag were fabricated and subjected to thermal annealing at 85 °C in a nitrogen ($N_2$) environment. As shown in Fig. 3a,c, thermal ageing of reference cells (denoted as Ref cells) over 138 hours revealed asymmetric degradation kinetics: fill factor (FF) decreased monotonically by 10%, while short-circuit density ($J_{SC}$) underwent an initial rapid drop (~25% within 20 hours, noted as typical 'burn-in' degradation) followed by partial recovery (15% of initial). The open-circuit voltage ($V_{OC}$) remains relatively stable (<5% variation), leading to a cumulative efficiency loss of 21% with final PCE = 79% of the initial. The rapid performance degradation upon thermal annealing in PM6:L8-BO cells is consistent with previous findings on PM6:Y6 devices[29], which is ascribed to interfacial degradation between the photoactive layer (PAL) and $MoO_3$. Time-of-flight secondary ion mass spectrometry (TOF-SIMS) results reveal acceptor enrichment at the top interface of the active layer (Supplementary Fig. 21c) and accumulation of $MoO_3$ on top of ZnO upon heating (Supplementary Fig. 21b), which explains the significant 'burn-in' performance decay. Following our previous findings[29,39], a

3-nm $C_{60}$ layer was deposited between the active layer and $MoO_3$ by thermal evaporation. As shown in Fig. 3b,c, the thin $C_{60}$ layer effectively suppresses the 'burn-in' degradation of the cells. TOF-SIMS results reveals that the $C_{60}$ layer also suppresses acceptor enrichment and $MoO_3$ diffusion/accumulation (Supplementary Fig. 21f,g). We therefore confirmed that the $C_{60}$ layer acts as a barrier that inhibits interfacial reactions and the diffusion of $MoO_3$ species during heating and consequently improves device thermal stability. Consequently, the devices with the $C_{60}$ layer (denoted as CMA cells) maintained 95% of their initial efficiency after 138 hours of heating at 85 °C, providing strong evidence for the role of the $C_{60}$ layer in improving thermal stability. Notably, devices with the $C_{60}$ layer exhibited an initial efficiency increase during the early stages of heating, primarily due to an improvement in FF. This can be attributed to the optimization of the PAL/$C_{60}$/$MoO_3$ interface, which enhances the interface charge dynamics.

We then assessed the performance variations of OPV cells with or without $C_{60}$ interlayer in both binary and $PC_{61}$PeA-incorporated ternary blends using different acceptors L8-BO, BTP-eC9, Y6 and BO-4Cl. As shown in Fig. 3d, the ternary cells incorporating $PC_{61}$PeA exhibited enhanced performance compared to their binary counterparts, with the PM6:BO-4Cl:$PC_{61}$PeA ternary device achieving a champion PCE of 18.6% (certified 18.0%; Supplementary Fig. 24), ranking among the highest efficiencies reported for inverted OPVs[19,20,40]. Figure 3e presents the performance evolution of these devices after annealing at 85 °C for 45 hours. In the binary reference cells without a $C_{60}$ protection layer (green symbols), significant 'burn-in' degradation was observed, which was successfully mitigated by the $C_{60}$ layer (CMA cells, red symbols). Similarly, ternary cells without $C_{60}$ protection (blue symbols) experienced 'burn-in' degradation, while the $C_{60}$ layer effectively suppressed this degradation (yellow symbols). Figure 3f,g depicts PCE evolution of different cells over 1,351 hours of thermal annealing at 85 °C and 150 °C, respectively. Devices incorporating the $C_{60}$ protection layer (yellow and red symbols) demonstrated superior thermal stability compared to their unprotected counterparts. It is worth noting that in comparison with their respective binary devices, ternary cells exhibited almost no PCE decay after 1,351 hours of thermal ageing at 85 °C, highlighting the stabilizing effect of the $PC_{61}$PeA additive. Increasing the annealing temperature to 150 °C accelerated PCE degradation, yet both the $C_{60}$ interlayer and $PC_{61}$PeA additive continued to enhance device stability. Among all devices, the interface-protected PM6:BO-4Cl:$PC_{61}$PeA cell retained 99% of its initial efficiency at 85 °C and 71% at 150 °C after 1,351 hours, whereas the interface-protected PM6:L8-BO cell maintained 95% at 85 °C and 42% at 150 °C under identical ageing conditions. We attributed the extreme high stability of the PM6:BO-4Cl:$PC_{61}$PeA cell to the synergetic effects of $PC_{61}$PeA in preventing the blend film from over crystallization and the $C_{60}$ layer in protecting the PAL/$MoO_3$ interface. Using the Arrhenius model (Supplementary Note 2)[41,42], the activation energy for degradation of the interface-protected PM6:BO-4Cl:$PC_{61}$PeA cell was estimated to be 0.52 eV, corresponding to a projected operational lifetime exceeding 25 years (Fig. 1b).

## Lateral water vapour diffusion

A good encapsulation is crucial for OPVs to withstand the harsh damp heat and thermal cycling conditions[37,43]. We selected ABT as the backsheet encapsulant due to its low cost, flexibility and excellent water barrier properties (Supplementary Fig. 27). Given that aluminium foil itself offers outstanding water barrier performance, lateral penetration from the side of the encapsulation layer emerges as the primary pathway for water diffusion. To date, only 1D diffusion models based on infinite edge lengths have been established by Michels et al.[44] for analysing lateral diffusion in encapsulated devices. This oversimplified model fails to capture practical applications of multidimensional moisture ingress pathways, particularly at geometric corners (Fig. 4a), a critical knowledge gap undermining encapsulation reliability predictions for electronics.

Optical calcium tests were performed with the ABT encapsulation to confirm and quantitively analyse the multidimensional water vapour diffusion process. Figure 4b depicts the ABT encapsulated 100-nm-thick square calcium (Ca) films on glass aged under 85 °C and 85% RH conditions (double 85 test). Figure 4c depicts the temporal evolution of calcium film corrosion, comparing the edge- and diagonal-displacement kinetics. As seen here, a linear correlation was measured for the calcium edge displacement related to the square root of time, both for the edge and the diagonal direction, which aligns with previously reported experimental observations[44–46].

The slope of this linear relationship is defined as the apparent diffusion rate $K$. Interestingly, both numerical simulations and experimental results confirm that the apparent diffusion rate $K$ along the diagonal ($K_{\mathrm{diag}}$) direction is approximately 1.54 times that along the edge ($K_{\mathrm{edge}}$; Supplementary Fig. 30 and Supplementary Table 9), highlighting a universally faster diffusion along the diagonal. A more detailed analysis of edge displacement kinetics revealed an increased calcium displacement rate along the edge after a critical point ($D_0$), indicating a shift in the diffusion mechanism. In this second stage, the apparent diffusion rate along the edge matches $K_{\mathrm{diag}}$, suggesting that beyond $D_0$, water vapour diffusion along the edge becomes equivalent to that along the diagonal. In other words, after reaching the critical point $D_0$, the moisture homogeneously diffuses within the film, corresponding well to the observed residual round shape of the calcium film. These findings confirm a two-dimensional (2D) diffusion process, where diagonal diffusion occurs 1.54 times faster than edge diffusion for water vapour. Consequently, relying solely on a 1D linear edge corrosion model would underestimate the actual water vapour diffusion rate. To achieve accurate estimations, it is essential to incorporate diagonal diffusion effects by applying a correction factor of 1.54.

The lateral diffusion of water vapour can occur via two distinct pathways: bulk diffusion within the adhesive layer and interface diffusion at the adhesive/substrate interface, which act synergistically in practical scenarios (Fig. 4d). Assuming that water vapour diffusion processes through the adhesive layer and interface follow the well-developed Fick model, the concentration equations for these two layers can be described as:

$$C_{\mathrm{A}}(x,t) = C_{\mathrm{SA}}\left(1-\mathrm{erf}\left(\frac{x}{2\sqrt{D_{\mathrm{A}}t}}\right)\right) \tag{1}$$

$$C_{\mathrm{I}}(x,t) = C_{\mathrm{SI}}\left(1-\mathrm{erf}\left(\frac{x}{2\sqrt{D_{\mathrm{I}}t}}\right)\right) \tag{2}$$

Where $C_{\mathrm{SA}}$ and $C_{\mathrm{SI}}$ are the saturation water vapour concentration at the adhesive and the interface and $D_{\mathrm{A}}$ and $D_{\mathrm{I}}$ represent the diffusion constants of water vapour through the adhesive and the interface, respectively.

Then, in a time difference ($\Delta T$) of calcium boundary moves from $L_0$ to $L_0 + \Delta L$, the total amount of water vapour ($N_{\mathrm{H2O}}$, in mol m$^{-1}$) that corrodes the calcium based on the reaction between calcium and water can be calculated to be:

$$N_{\mathrm{H_2O}} = \frac{2\Delta L h_{\mathrm{Ca}}\rho_{\mathrm{Ca}}}{M_{\mathrm{Ca}}} \tag{3}$$

Where $h_{\mathrm{Ca}}$ is the thickness of the calcium film, $\rho_{\mathrm{Ca}}$ is the density of calcium, $M_{\mathrm{Ca}}$ is the molar mass of calcium.

Meanwhile, the total amount of water vapour reaching the calcium edge through the bulk adhesive ($J_{\mathrm{A}}$) and the interface ($J_{\mathrm{I}}$) (in mol m$^{-1}$) during the period $\Delta T$ can be calculated to be:

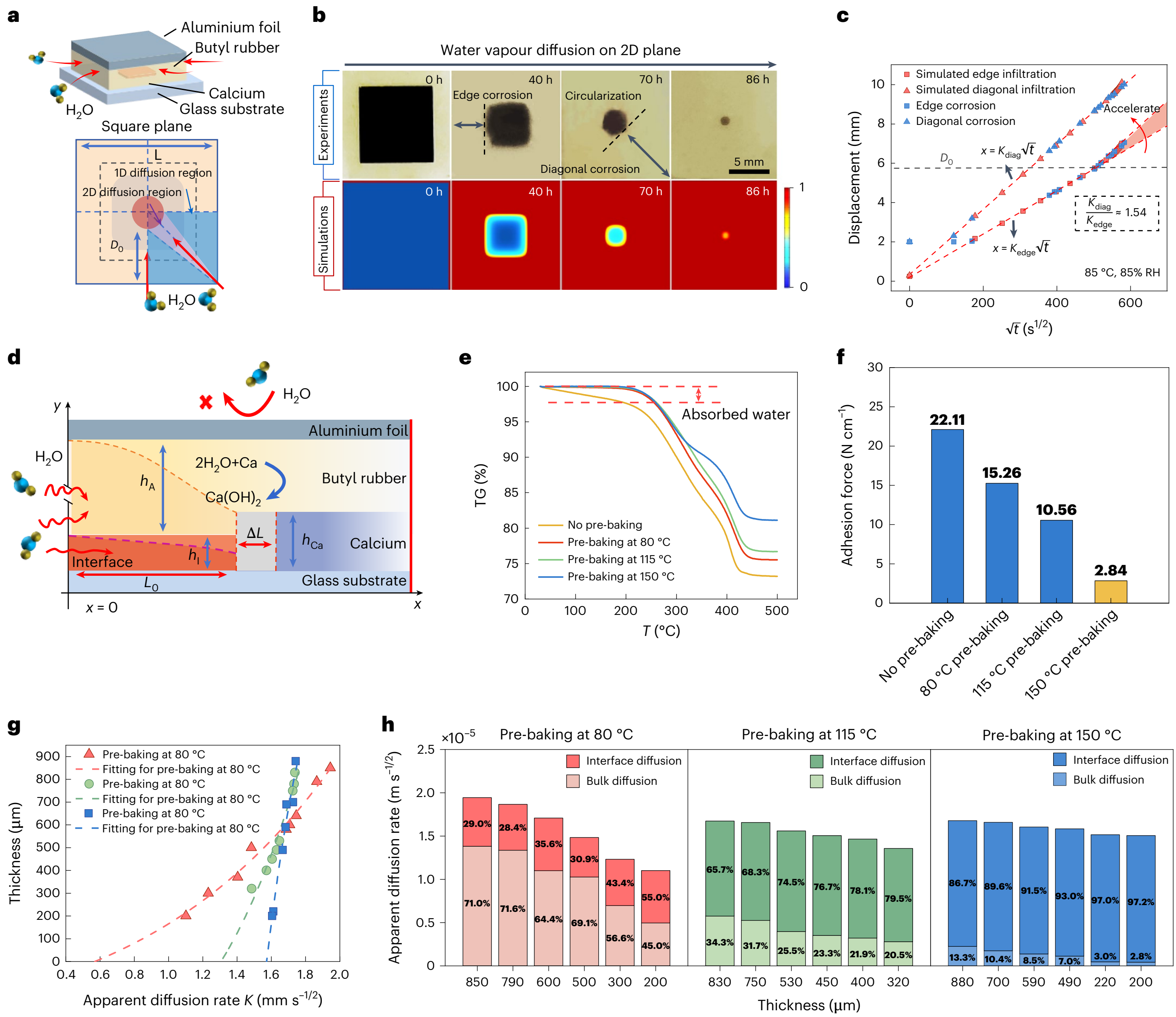

**Fig. 4 | Mechanisms of lateral diffusion of water vapour. a**, Schematic of 2D diffusion of water vapour. Three-dimensional schematic diagram (top) and 2D plan schematic diagram (bottom). $D_0$ represents the distance from the edge when the square calcium film is corroded by water into a circular shape. **b**, Optical photographs of calcium corrosion and finite element simulation results of water vapour diffusion. The colour scale bar indicates the relative concentration of water vapour. **c**, Plots of the calcium corrosion displacement versus square root of ageing time for the experiment (blue colour) and simulated (red colour) results. The curves are obtained by segmented linear fitting. The formulas describe the linear relationship between displacement and square root of ageing time. $K_{diag}$ represents the apparent diffusion coefficient for diagonal diffusion. $K_{edge}$ represents the apparent diffusion coefficient for edge diffusion. $t$ represents the diffusion time. **d**, Schematic diagram of a 1D water vapour lateral diffusion model. $h_A$ represents the thickness of the adhesive layer, $h_I$ represents the average effective thickness of water-permeable channels formed at the interface by the defects at the imperfect adhesive/substrate interface. $h_{Ca}$ represents the thickness of the calcium film. $L_0$ represents the initial distance from the edge of the calcium film to the edge of the encapsulation layer. $\Delta L$ represents the displacement of the calcium film. **e**, Thermogravimetric curves of butyl rubbers pre-baked at different temperatures. $T$ represents temperature. **f**, Adhesion of ABT encapsulants pre-baked at different temperatures. **g**, Variation of apparent water permeation rate $K$ with the thickness of butyl rubber, fitted with equation (9). **h**, Apparent diffusion rate $K$ at different adhesion forces and different thicknesses, and the percentage of bulk diffusion and interface diffusion.

$$J_A = \int_{L_0+\Delta L}^{\infty} h_A\, C_A(x,\, T_0+\Delta T)\, dx - \int_{L_0}^{\infty} h_A\, C_A(x,\, T_0)\, dx \quad (4)$$

$$J_I = \int_{L_0+\Delta L}^{\infty} h_I\, C_I(x,\, T_0+\Delta T)\, dx - \int_{L_0}^{\infty} h_I\, C_I(x,\, T_0)\, dx \quad (5)$$

Where $h_A$ is the thickness of the adhesive layer and $h_I$ represents the average effective thickness of water-permeable channels formed at the interface by the defects at the imperfect adhesive/substrate interface (Supplementary Note 4).

Solving the equations leads to (Supplementary Note 4):

$$J_A = \frac{2\sqrt{D_A T_0}}{L_0} C_{SA} h_A \left( \frac{e^{-\left(\frac{L_0}{2\sqrt{D_A T_0}}\right)^2}}{\sqrt{\pi}} - \frac{L_0}{2\sqrt{D_A T_0}} \operatorname{erfc}\left(\frac{L_0}{2\sqrt{D_A T_0}}\right) \right) \quad (6)$$

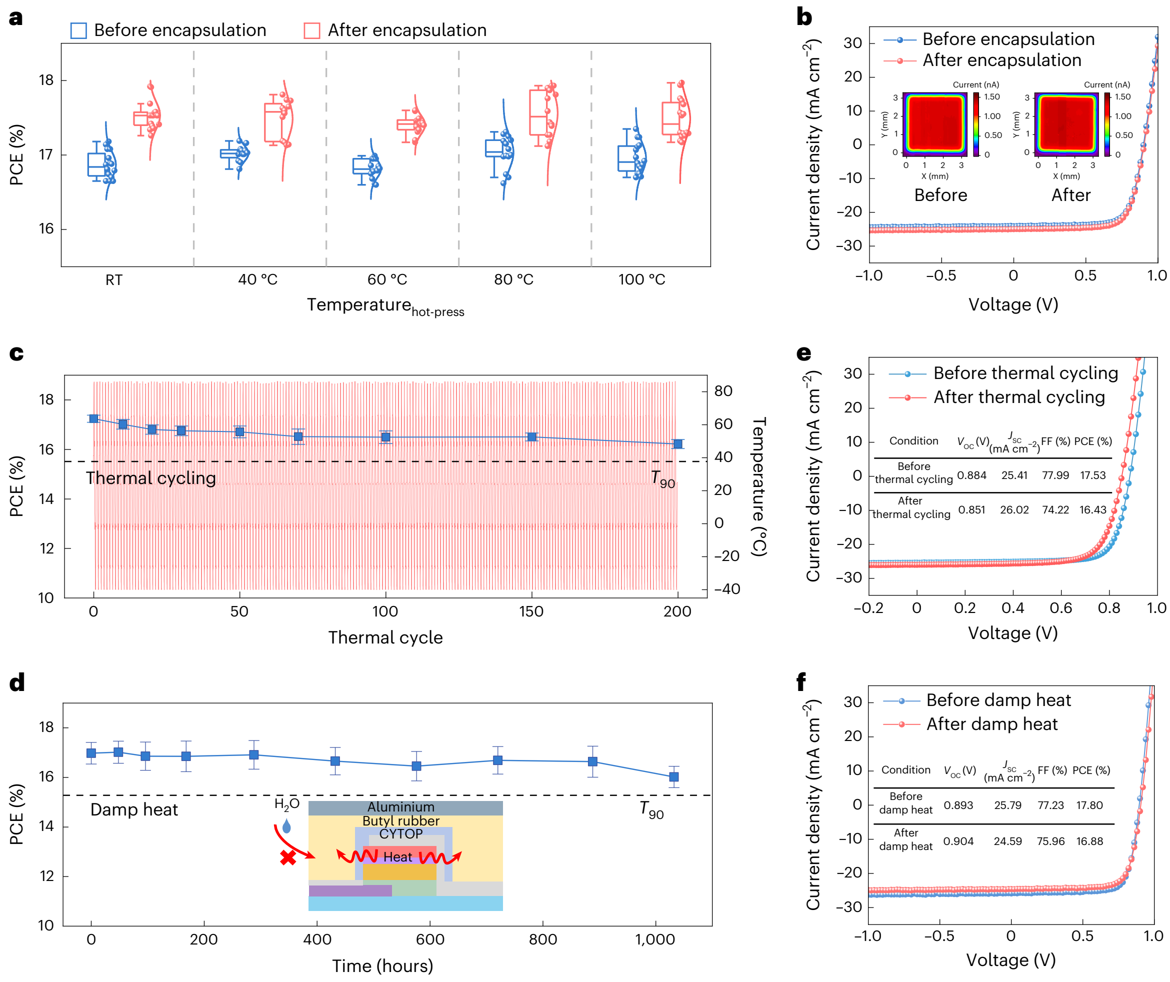

| Condition | $V_{OC}$ (V) | $J_{SC}$ (mA cm$^{-2}$) | FF (%) | PCE (%) |
|---|---|---|---|---|
| Before thermal cycling | 0.884 | 25.41 | 77.99 | 17.53 |
| After thermal cycling | 0.851 | 26.02 | 74.22 | 16.43 |

| Condition | $V_{OC}$ (V) | $J_{SC}$ (mA cm$^{-2}$) | FF (%) | PCE (%) |
|---|---|---|---|---|
| Before damp heat | 0.893 | 25.79 | 77.23 | 17.80 |
| After damp heat | 0.904 | 24.59 | 75.96 | 16.88 |

**Fig. 5 | Encapsulation and stability testing of high-efficiency inverted organic solar cells. a**, Statistical PCE of the PM6:L8-BO cells before and after encapsulated at different temperatures. The box plots show the minimum, maximum, median and first and third quartiles. Specifically, the centre line represents the median (50th percentile); the bounds of the box indicate the first (25th percentile) and third (75th percentile) quartiles; the whiskers extend to the minimum and maximum values. The statistical results are based on at least six individual devices. The dashed lines serve as a guide to separate data clusters. **b**, Representative *J*–*V* curves of the PM6:L8-BO cells before and after hot-press encapsulation at 100 °C; the insets are the LBIC images of the cell before and after encapsulation. **c**,**d**, PCE evolution of the PM6:L8-BO cells under 200 thermal cycling tests (−40 °C to 85 °C) (**c**) and 1,032 hours damp heat test (at 85 °C, 85% RH) (**d**). The inset shows a diagram of the device structure. The centre of the error bar is defined as the average value, and error bar is defined as the standard deviation, which is calculated from the statistical results of at least eight individual devices. The dashed lines indicate the 90% threshold of the average device efficiency. **e**,**f**, Representative *J*–*V* curves and performance parameters of organic solar cells before and after 200 thermal cycling tests (**e**) and 1,032 hours damp heat test (**f**).

$$J_{\mathrm{I}}=\frac{2\sqrt{D_{\mathrm{I}}T_0}}{L_0}C_{\mathrm{SI}}h_{\mathrm{I}}\left(\frac{\mathrm{e}^{-\left(\frac{L_0}{2\sqrt{D_{\mathrm{I}}T_0}}\right)^2}}{\sqrt{\pi}}-\frac{L_0}{2\sqrt{D_{\mathrm{I}}T_0}}\mathrm{erfc}\left(\frac{L_0}{2\sqrt{D_{\mathrm{I}}T_0}}\right)\right)\qquad(7)$$

where erfc is the complementary error function. Since calcium corrosion comes only from the water vapour erosion, the total amount of water vapour for calcium corrosion should be equal to the total amount of water vapour passing through the bulk adhesive and the interface, that is:

$$N_{H_2O}=J_{\mathrm{A}}+J_{\mathrm{I}}\qquad(8)$$

Combining equations (3), (6) and (7), a relationship between the apparent diffusion rate of water vapour *K* and the thickness of the adhesive layer $h_{\mathrm{A}}$ is obtained (more details in Supplementary Note 4):

$$h_{\mathrm{A}}=\frac{K\left(N_0-\frac{2\sqrt{D_{\mathrm{I}}}}{K}C_{\mathrm{SI}}h_{\mathrm{I}}\frac{1}{\sqrt{\pi}}\right)}{2\sqrt{D_{\mathrm{A}}}\,C_{\mathrm{SA}}\left(\frac{1}{\sqrt{\pi}}+\frac{K^2}{4\sqrt{\pi}D_{\mathrm{A}}}-\frac{K}{2\sqrt{D_{\mathrm{A}}}}\right)}\qquad(9)$$

Pre-annealing ABT encapsulants removes the adsorbed water from butyl rubber (as shown in Fig. 4e) while reducing the bond strength of ABT encapsulants to the substrate (as shown in Fig. 4f; Supplementary Note 3 provides test method), providing excellent encapsulation models with different fractions of bulk diffusion and interface diffusion. One-hundred-nm-thick calcium films were then encapsulated with ABT encapsulants with different thicknesses through hot pressing, and the corrosion process of the encapsulated calcium was tested under double 85 testing conditions. The calcium edge corrosion versus time is shown in Supplementary Figs. 33–35. The calcium corrosion is consistent with the coexistence of 1D and 2D corrosion processes described above. Using the edge corrosion process, the apparent diffusion rates *K* of adhesives with different thicknesses and annealing temperatures were obtained, and the results are listed in Supplementary Table 11. The experimental results of $K$ vs $h_A$ are given in Fig. 4g, along with the fitted curves based on equation (9). The values of the parameters obtained from the fitting are listed in Supplementary Table 10. Various layer thicknesses and adhesive properties of the ABT encapsulants were tested; the experimental results fit well to equation (9) with a fitted $R^2$ date of 0.96–0.99, indicating that the established model is reasonable and can be used to quantitatively analyse the lateral water vapour diffusion. The fitted $D_A$ is in the order of $10^{-10}$ $m^2$ $s^{-1}$, which is in good accordance with literature reports[47]. $D_A$ decreased one order of magnitude with the increase of annealing temperature, which can be ascribed to the cross-linking effect of the butyl rubber under high temperatures that lower the diffusion rate.

According to equations (6) and (7), the respective contribution shares of bulk diffusion and interface diffusion were calculated, and the results are shown in Fig. 4h. As seen here, for the ABT encapsulants with better interface adhesion, much lower interfacial diffusion contribution was measured (29%–55%, 66%–80% and 87%–97% for the films annealed at 80 °C, 115 °C and 150 °C, respectively). Not surprisingly, lowering the adhesive layer thickness decreases the contribution of the bulk diffusion and the consequent $K$ value when the interfacial adhesive is good enough. In contrast, poor interface adhesion yields a high contribution to interfacial water vapour diffusion, and no significant adhesive layer thickness dependence was measured.

On the basis of the established in-plane 2D diffusion and 1D lateral penetration models for moisture in encapsulated solar cells, two key findings emerge: (1) 2D diffusion accelerates moisture penetration by a factor of 1.54, leading to rapid corner corrosion in real applications. Therefore, it is essential to consider 2D diffusion when calculating the width of the edge encapsulant; (2) lateral diffusion of moisture is governed by the encapsulant layer thickness ($h_A$), water diffusivity in the encapsulant ($D_A$) and the imperfection of the interface ($h_I$). Reducing the layer thickness of the encapsulant and enhancing the interface adhesive would yield better encapsulation. In this study, organic solar cells were then encapsulated using ABT films with a 200-µm thickness, following pre-annealing at 80 °C to remove the absorbed water. Together with the established faster 2D diffusion along the diagonal direction, a minimal edge width of 22.7 mm is calculated to fully protect our cell from corrosion over 1,000 hours in the double 85 test, which was applied to the following cell encapsulation process (Supplementary Note 5).

## OPV encapsulation and reliability tests

The intrinsically stable inverted OPVs based on PM6:L8-BO blends with a $C_{60}$ interface-protection layer were encapsulated with ABT encapsulants for damp heat and thermal cycling tests. Figure 5a presents the statistical PCE data of the devices before and after encapsulation at different hot-pressing temperatures (detailed performance data available in Supplementary Table 12). The current density–voltage ($J$–$V$) characteristic of a device encapsulated at 100 °C is shown in Fig. 5b. Notably, across a broad range of hot-press temperatures, device performance exhibited a slight improvement (~3.5%) after encapsulation, attributed to the optimization of the PAL/$C_{60}$/$MoO_3$ interface through thermal heating (*vide supra*). Laser beam induced current (LBIC) images before and after hot-press encapsulation (the inset of Fig. 5b) show minimal variation, confirming that the hot-press encapsulation method does not degrade device performance. To assess the long-term stability of the encapsulated OPVs, 200 thermal cycling tests were conducted following the ISOS-T-3 standards, including thermal cycling at temperatures between −40 °C and 85 °C at a relative humidity of <55%. The test results are shown in Fig. 5c. The $J$–$V$ characteristics of the representative cell before and after 200 thermal cycles are shown in Fig. 5e. After 200 cycles, the devices maintained 94% of their initial efficiency, demonstrating excellent stability in accordance with ISOS-T-3 test standard.

We then performed a rigorous damp heat test on the devices. Figure 5d shows the efficiency changes of the devices over 1,000 hours of damp heat testing, with the representative $J$–$V$ curves before and after ageing shown in Fig. 5f. Encouragingly, statistical data showed that the tested cells maintained over 94% of their initial efficiency after 1,032 hours of damp heat testing. The test complies with the ISOS-D-3 standard, marking the high stability of these high-efficiency inverted OPVs under a damp heat test.

The superior thermal cycling and damp heat stability observed can be attributed to both the high intrinsic thermal stability of the optimized devices and the excellent encapsulation performance of the ABT encapsulants. Additionally, ABT encapsulants exhibit remarkable mechanical flexibility. Leveraging this property, we successfully encapsulated flexible OPVs that retained 97% of their initial efficiency after 10,000 inward and outward bending cycles with a radius of 5 mm (Supplementary Fig. 39). This study establishes a robust framework for environmentally resilient OPVs, demonstrating industrial-standard reliability under combined thermal and humidity stresses, while also preserving mechanical flexibility for versatile applications.

## Conclusion

To achieve highly stable OPV devices, it is necessary to get simultaneous breakthroughs in material design and screening, understanding intrinsic device degradation and encapsulation engineering. In this work, we proved a systematic approach from three levels to enhance OPVs stability: (1) definition of the active layer morphological transition onset temperature ($T_{onset}$) via UV–vis spectroscopy, proposing $T_{onset}$ as a universal descriptor for intrinsic thermal stability of organic semiconductors and establishing a rapid screening criterion enabling rational material selection for stable OPVs; (2) elucidation of the interface-dominated degradation mechanism and its mitigation via $C_{60}$ interfacial protection, enabling OPVs with excellent stability through the combination of a stable active layer and stable interface; (3) development of the first two-dimensional planar and edge moisture diffusion kinetic models, creating a multidimensional moisture diffusion framework that revolutionizes encapsulation design principles. The resulting encapsulation strategy—combining optimized adhesive layers and interface passivation—delivers outstanding stability under damp heat (ISOS-D-3) and thermal cycling (ISOS-T-3) tests. These findings overcome long-standing stability bottlenecks and provide a methodological template for stabilizing emerging flexible energy technologies. Future work will extend this stability paradigm to large-area modules and develop printable barrier-based thin-film encapsulation to reduce costs.

## Methods

### Materials

PM6 (PBDB-T-2F), L8-BO, BO-4Cl, Y6 and BTP-eC9 were purchased from Hyper, Inc. [6,6]-phenyl-$C_{61}$-pentyl acrylate ($PC_{61}PeA$) was synthesized using the method from our previous work[22]. 1,4-Diiodobenze was purchased from TCI Development Co., Ltd. Molybdenum (VI) oxide ($MoO_3$) was purchased from Strem Chemicals. $Zn(OAc)_2$ and KOH were purchased from J&K Scientific. ZnO nanoparticle solution was prepared through the reaction between KOH and $Zn(OAc)_2$ in MeOH. All materials were used as received without further purification.

### Fabrication of inverted solar cells and characterization

ITO substrates were sequentially cleaned by detergent, deionized water and ethanol twice in an ultrasound cleaner. Before using them, they were dried under a $N_2$ flow and then treated in an ultraviolet–ozone oven for 30 min. First, ZnO nanoparticles (15 mg $ml^{-1}$ in methanol) were spin coated on the ITO substrates at 3,000 r.p.m. for 30 s and then were annealed at 130 °C for 10 min. The mixed solution of PM6:L8-BO, PM6:BO-4Cl, PM6:Y6 and PM6:BTP-eC9 (1:1.2 w/w, 7 mg $ml^{-1}$ in total) in chloroform with 1,4-diiodobenzene as a solid additive (the content of 1,4-diiodobenzene is 50% of the total mass of the donor and acceptor) was stirred at 55 °C for 2 h. Then, PM6:L8-BO, PM6:BO-4Cl, PM6:Y6 and PM6:BTP-eC9 was spin coated on top of the ZnO ETL at 2,500 r.p.m. for 60 s and then annealed at 85 °C for 10 min on a hot plate in a $N_2$-filled glovebox. The mixed solution of PM6:L8-BO:$PC_{61}$PeA, PM6:BO-4Cl:$PC_{61}$PeA, PM6:Y6:$PC_{61}$PeA and PM6:BTP-eC9:$PC_{61}$PeA (1:1.2:0.5 w/w, 7 mg ml$^{-1}$ in total) in chloroform with 1,4-diiodobenzene as a solid additive (the content of 1,4-diiodobenzene is 50% of the total mass of the donor and acceptor) was stirred at 55 °C for 2 h. Then, PM6:L8-BO:$PC_{61}$PeA, PM6:BO-4Cl:$PC_{61}$PeA, PM6:Y6:$PC_{61}$PeA and PM6:BTP-eC9:$PC_{61}$PeA was spin coated on top of the ZnO ETL at 2,500 r.p.m. for 60 s and then annealed at 160 °C for 5 min on a hot plate in a $N_2$-filled glovebox. Then $C_{60}$ (3 nm) was evaporated as a protective layer. Finally, $MoO_3$ (10 nm) as the hole extraction layer and Ag (100 nm) as the anode were sequentially vacuum deposited on top of the active layer, respectively. The effective photovoltaic area, defined by the geometrical overlap between the bottom cathode electrode and the top anode, was 4 mm$^2$ and 9 mm$^2$.

The photovoltaic parameters of the cells, including $V_{OC}$, $J_{SC}$ and FF, were measured using a Keithley 2400 source meter under air mass 1.5 global (AM1.5 G; 100 mW cm$^{-2}$) illumination provided by a solar simulator (Zolix SS150A) in a $N_2$-filled glovebox at 25 °C. The cells are measured in the forward direction with a step of 0.02 V and the dwell time is 0.1 s for every point in our laboratory. The light intensity of the solar simulator for $J$–$V$ measurement was calibrated with a reference silicon cell (QE-B1, Zolix). The designated illumination area defined by a thin metal mask of 2.56 mm$^2$ and 6.25 mm$^2$.

The external quantum efficiency spectra were recorded by a custom-built external quantum efficiency system, and light from a 150 W tungsten halogen lamp (Osram 64610) was used as a probe light and was modulated with a mechanical chopper before passing through the monochromator (Zolix, Omni-k300) to select the wavelength. The response was recorded as the voltage by an $I$–$V$ converter (D&R-IV converter, Suzhou D&R Instruments), using a lock-in amplifier (Stanford Research Systems SR830) with a standard silicon cell as the reference before testing the devices.

### UV–vis absorption spectroscopic characterization

The active layer films used for testing were prepared under conditions consistent with those used for active layer films in optimal performance devices. The active layer films used for testing were pre-annealed before testing to approximate the molecular motions of the films as they would be in the actual devices. The absorption spectra of films were tested by a Lambda 750 UV/vis/near-infrared spectrophotometer (PerkinElmer). Measurements were made over a wavelength range of 300 to 1,000 nm, with sampling increments of 1 nm (the original slide was used as the absorption baseline). A holder was used to fix the test position of each sample to minimize errors during the test. Heating during testing was performed on a hot plate in a nitrogen glovebox for five minutes and cooled to room temperature (~25 °C) before testing.

### GIWAXS characterization

The GIWAXS measurements were characterized by the Xeuss SAXS/WAXS 3.0 system (Xenocs) with an X-ray wavelength of 1.341 Å at Vacuum Interconnected Nanotech Workstation (Nano-X) of SINANO.

### LBIC mapping

A home-built apparatus was utilized to obtain LBIC images. This apparatus comprised a 5 mW, 532 nm green monochromatic laser diode that generated a 3-μm diameter laser beam, which was attached to a moving X–Y stage that was controlled by a computer. Simultaneously, cell output currents were measured by a source measurement unit (2602 Keithley) while the cell surface was scanned. The entire active area of the cell was scanned, a process that took approximately 30 minutes.

### TOF-SIMS characterization

The TOF-SIMS data were tested using TOF-SIMS5-100. Inverted devices of the PM6:L8-BO system and PM6:BO-4Cl:$PC_{61}$PeA system with and without a $C_{60}$ interfacial layer were prepared and heated at 150 °C for different times. Various elements including Ag, Mo, O, S, SN and Zn were detected using anionic mode for their distribution.

### Device encapsulation

Aluminium foil butyl tape (ABT) encapsulant was purchased from China Railway Weiye Waterproof Material Technology Co., Ltd. ABT encapsulants were de-watered by pre-baking on a hot plate in a $N_2$ glovebox before use. The ABT encapsulant was laminated to the device surface and pressed to the device surface by a stroke-controlled hot press (HP-Lab-10, Suzhou D&R Instruments). The hot-press temperature was set from room temperature to 100 °C as shown in the literature. The press time was set to 5 min. After the press was completed, the spilled butyl rubber was cleaned up so as not to interfere with the test. To further improve the water resistance of the encapsulant and protect the device, a thin layer of perfluoropolymer (CYTOP) was applied to the device before applying the encapsulant.

### Reliability test

The devices were stored in a climate chamber (D&R PVLT-9001-16A, Suzhou D&R Instruments) maintained at 85 °C/85% RH for long-term damp heat stability experiments. These samples were only removed from the chamber for $J$–$V$ scanning and put back immediately after the measurements.

For thermal cycling testing, the climate chamber temperature is programmed to vary between -40 °C and 85 °C. The relative humidity in the chamber was maintained above 85%. The temperature variation curve is shown in Fig. 5b. The temperature of the climate chamber was set to return to room temperature every ten cycles so that the devices could be removed for $J$–$V$ scanning and returned immediately after the measurements. Bending tests of the flexible devices were performed by a bending machine (FlexTest-TM-L) with a bending radius of 5 mm. Ten thousand inward and outward bends were performed on the flexible devices. The device was removed every 2,000 bends to scan the $J$–$V$.

### Optical calcium test

Optical calcium tests were used to characterize the lateral diffusion of water vapour. Square calcium films with 11-mm side lengths were deposited on square glass sheets with 24.5-mm side lengths, and ABT encapsulants with 15-mm side lengths were cut to encapsulate the calcium films. Stroke-controlled hot-press equipment (HP-Lab-10, Suzhou D&R Instruments) was used to press laminate the ABT encapsulant to the substrate and control the thickness of the adhesive layer. The encapsulated calcium films were placed in a climate chamber at 85 °C/85% RH. The corrosion of calcium by water vapour penetration was recorded by a camera. The displacement of the calcium film during corrosion was measured by ImageJ.

### Finite element simulation

The finite element simulations are carried out using the dilute matter transfer module in COMSOL, and the simulations satisfy the Fick's law of diffusion.

### Water vapour transmission rate characterization

The water vapour permeability was measured using a water vapour transmission rate permeation analyser (AQUATRAN MODEL 2, AMETEK MOCON). The sample was positioned between two chambers with different partial pressures of water vapour, and the vapour flux through the sample was measured.

### Reporting summary

Further information on research design is available in the Nature Portfolio Reporting Summary linked to this article.

## Data availability

All data needed to evaluate the conclusions in this paper are present in the Article and its Supplementary Information. Source data are provided with this paper.

## References

1. Cardinaletti, I. et al. Organic and perovskite solar cells for space applications. *Sol. Energy Mater. Sol. Cells* **182**, 121–127 (2018).
2. Müller-Buschbaum, P. Testing flexible polymer solar cells in near-space. *Natl Sci. Rev.* **10**, nwad071 (2023).
3. Xu, Z. et al. In-situ performance and stability tests of large-area flexible polymer solar cells in the 35-km stratospheric environment. *Natl Sci. Rev.* **10**, nwac285 (2023).
4. Meitzner, R., Schubert, U. S. & Hoppe, H. Agrivoltaics—the perfect fit for the future of organic photovoltaics. *Adv. Energy Mater.* **11**, 2002551 (2021).
5. Song, W. et al. Semi-transparent organic photovoltaics for agrivoltaic applications. *Nano Energy* **116**, 108805 (2023).
6. Li, Y., Huang, X., Sheriff, H. K. Jr & Forrest, S. R. Semitransparent organic photovoltaics for building-integrated photovoltaic applications. *Nat. Rev. Mater.* **8**, 186–201 (2023).
7. Panidi, J., Georgiadou, D. G., Schoetz, T. & Prodromakis, T. Advances in organic and perovskite photovoltaics enabling a greener Internet of Things. *Adv. Funct. Mater.* **32**, 2200694 (2022).
8. Suthar, R., Dahiya, H., Karak, S. & Sharma, G. D. Indoor organic solar cells for low-power IoT devices: recent progress, challenges, and applications. *J. Mater. Chem. C* **11**, 12486–12510 (2023).
9. Chen, C. et al. Molecular interaction induced dual fibrils towards organic solar cells with certified efficiency over 20%. *Nat. Commun.* **15**, 6865 (2024).
10. Jiang, Y. et al. Non-fullerene acceptor with asymmetric structure and phenyl-substituted alkyl side chain for 20.2% efficiency organic solar cells. *Nat. Energy* **9**, 975–986 (2024).
11. Zhu, L. et al. Achieving 20.8% organic solar cells via additive-assisted layer-by-layer fabrication with bulk p-i-n structure and improved optical management. *Joule* **8**, 3153–3168 (2024).
12. Zhang, T. et al. A medium-bandgap nonfullerene acceptor enabling organic photovoltaic cells with 30% efficiency under indoor artificial light. *Adv. Mater.* **34**, 2207009 (2022).
13. Wang, W. et al. High-performance organic photovoltaic cells under indoor lighting enabled by suppressing energetic disorders. *Joule* **7**, 1067–1079 (2023).
14. Jiang, Y. et al. Photocatalytic effect of ZnO on the stability of nonfullerene acceptors and its mitigation by $SnO_2$ for nonfullerene organic solar cells. *Mater. Horiz.* **6**, 1438–1443 (2019).
15. Liu, B. et al. Visible light–induced degradation of inverted polymer:nonfullerene acceptor solar cells: initiated by the light absorption of ZnO layer. *Sol. RRL* **5**, 2000638 (2020).
16. Liu, B. W. et al. Simultaneously achieving highly efficient and stable polymer:non-fullerene solar cells enabled by molecular structure optimization and surface passivation. *Adv. Sci.* **9**, e2104588 (2022).
17. Ding, K., Li, Y. & Forrest, S. R. Characterizing and improving the thermal stability of organic photovoltaics based on halogen-rich non-fullerene acceptors. *ACS Appl. Mater. Interfaces* **14**, 5692–5698 (2022).
18. Li, Y. et al. Non-fullerene acceptor organic photovoltaics with intrinsic operational lifetimes over 30 years. *Nat. Commun.* **12**, 5419 (2021).
19. Huang, J. et al. 19.5% inverted organic photovoltaic with record long-lifetime via multifunctional interface engineering featuring radical scavenger. *Nat. Commun.* **15**, 10565 (2024).
20. Suo, Z. C. et al. A water solution processed hybrid electron transport layer simultaneously enhances efficiency and stability in inverted structure organic solar cells. *Adv. Funct. Mater.* **34**, 2409699 (2024).
21. Qin, Y. et al. The performance-stability conundrum of BTP-based organic solar cells. *Joule* **5**, 2129–2147 (2021).
22. Song, H. et al. Simultaneously enhancing efficiency and thermo-/UV-stability of organic solar cells by regulating the nanomorphology of the polymer blend by an acrylated fullerene derivative. *Chem. Eng. J.* **503**, 158694 (2025).
23. Sheriff, H. K. M., Li, Y., Arneson, C. E. & Forrest, S. R. Reliability of colorfast semitransparent organic photovoltaics. *Device* **2**, 100369 (2024).
24. Reese, M. O. et al. Consensus stability testing protocols for organic photovoltaic materials and devices. *Sol. Energy Mater. Sol. Cells* **95**, 1253–1267 (2011).
25. Guo, Q. et al. Asymmetrically noncovalently fused-ring acceptor for high-efficiency organic solar cells with reduced voltage loss and excellent thermal stability. *Nano Energy* **74**, 104861 (2020).
26. Li, W., Liu, D. & Wang, T. Stability of non-fullerene electron acceptors and their photovoltaic devices. *Adv. Funct. Mater.* **31**, 2104552 (2021).
27. Min, J. et al. Side-chain engineering for enhancing the properties of small molecule solar cells: a trade-off beyond efficiency. *Adv. Energy Mater.* **6**, 1600515 (2016).
28. Yang, W. et al. Simultaneous enhanced efficiency and thermal stability in organic solar cells from a polymer acceptor additive. *Nat. Commun.* **11**, 1218 (2020).
29. Qin, X. et al. Thermal-induced performance decay of the state-of-the-art polymer: non-fullerene solar cells and the method of suppression. *Molecules* **28**, 6856 (2023).
30. Sung, Y.-M., Huang, Y.-C., Chien, F. S.-S. & Tsao, C.-S. Mechanism and analysis of thermal burn-in degradation of OPVs induced by evaporated HTL. *IEEE J. Photovolt.* **9**, 694–699 (2019).
31. Yin, Y., Pan, X., Andersson, M. R., Lewis, D. A. & Andersson, G. G. Mechanism of organic solar cell performance degradation upon thermal annealing of $MoO_x$. *ACS Appl. Energy Mater.* **3**, 366–376 (2019).
32. Sachs-Quintana, I. T. et al. Electron barrier formation at the organic-back contact interface is the first step in thermal degradation of polymer solar cells. *Adv. Funct. Mater.* **24**, 3978–3985 (2014).
33. Balcaen, V., Rolston, N., Dupont, S. R., Voroshazi, E. & Dauskardt, R. H. Thermal cycling effect on mechanical integrity of inverted polymer solar cells. *Sol. Energy Mater. Sol. Cells* **143**, 418–423 (2015).
34. Dupont, S. R., Novoa, F., Voroshazi, E. & Dauskardt, R. H. Decohesion kinetics of PEDOT: PSS conducting polymer films. *Adv. Funct. Mater.* **24**, 1325–1332 (2014).
35. Lee, C.-Y. et al. Encapsulation improvement and stability of ambient roll-to-roll slot-die-coated organic photovoltaic modules. *Sol. Energy* **213**, 136–144 (2021).
36. Qin, J. et al. In situ solution-processed submicron thick $SiO_xC_y$/a-$SiN_x$(O):H composite barrier film for polymer:non-fullerene photovoltaics. *Small Methods* **7**, 2300224 (2023).
37. Sutherland, L. J., Weerasinghe, H. C. & Simon, G. P. A review on emerging barrier materials and encapsulation strategies for flexible perovskite and organic photovoltaics. *Adv. Energy Mater.* **11**, 2101383 (2021).
38. Root, S. E., Alkhadra, M. A., Rodriquez, D., Printz, A. D. & Lipomi, D. J. Measuring the glass transition temperature of conjugated polymer films with ultraviolet–visible spectroscopy. *Chem. Mater.* **29**, 2646–2654 (2017).

39. Xi, Q. et al. Improving the thermal stability of inverted organic solar cells by mitigating the undesired $MoO_3$ diffusion toward cathodes with a high-ionization potential interface layer. *ACS Appl. Mater. Interfaces* **17**, 15456–15467 (2025).
40. Liu, B. et al. Inverted organic solar cells with an in situ-derived $SiO_xN_y$ passivation layer and power conversion efficiency exceeding 18%. *Nat. Photonics* **19**, 195–203 (2025).
41. Adams, J. et al. Water ingress in encapsulated inverted organic solar cells: correlating infrared imaging and photovoltaic performance. *Adv. Energy Mater.* **5**, 1501065 (2015).
42. Schuller, S., Schilinsky, P., Hauch, J. & Brabec, C. J. Determination of the degradation constant of bulk heterojunction solar cells by accelerated lifetime measurements. *Appl. Phys. A* **79**, 37–40 (2004).
43. Ahmad, J., Bazaka, K., Anderson, L. J., White, R. D. & Jacob, M. V. Materials and methods for encapsulation of OPV: a review. *Renew. Sustain. Energy Rev.* **27**, 104–117 (2013).
44. Michels, J. J., Peter, M., Salem, A., van Remoortere, B. & van den Brand, J. A combined experimental and theoretical study on the side ingress of water into barrier adhesives for organic electronics applications. *J. Mater. Chem. C* **2**, 5759–5768 (2014).
45. Kempe, M. D., Dameron, A. A. & Reese, M. O. Evaluation of moisture ingress from the perimeter of photovoltaic modules. *Prog. Photovoltaics Res. Appl.* **22**, 1159–1171 (2013).
46. Kempe, M. D., Panchagade, D., Reese, M. O. & Dameron, A. A. Modeling moisture ingress through polyisobutylene-based edge-seals. *Prog. Photovolt.* **23**, 570–581 (2014).
47. Krongauz, V. V., Bennett, S. E. & Ling, M. T. K. Kinetics of water vapor diffusion in resins. *J. Therm. Anal. Calorim.* **125**, 231–243 (2016).
48. Cheng, X., Marstein, E. S., Haug, H., You, C. C. & Di Sabatino, M. Thermal stability of hydrogenated amorphous silicon passivation for p-type crystalline silicon. *Phys. Status Solidi A* **213**, 91–95 (2015).
49. Khadka, D. B., Shirai, Y., Yanagida, M., Uto, K. & Miyano, K. Analysis of degradation kinetics of halide perovskite solar cells induced by light and heat stress. *Sol. Energy Mater. Sol. Cells* **246**, 111899 (2022).
50. Kim, J. et al. An effective method of predicting perovskite solar cell lifetime–case study on planar $CH_3NH_3PbI_3$ and $HC(NH_2)_2PbI_3$ perovskite solar cells and hole transfer materials of spiro-OMeTAD and PTAA. *Sol. Energy Mater. Sol. Cells* **162**, 41–46 (2017).
51. Núñez, N., González, J. R., Vázquez, M., Algora, C. & Espinet, P. Evaluation of the reliability of high concentrator GaAs solar cells by means of temperature accelerated aging tests. *Prog. Photovolt.* **21**, 1104–1113 (2012).
52. Zhao, X. et al. Operationally stable perovskite solar modules enabled by vapor-phase fluoride treatment. *Science* **385**, 433–438 (2024).
53. Ma, Y. et al. Understanding microstructural development of perovskite crystallization for high performance solar cells. *Adv. Mater.* **35**, 2306947 (2023).
54. Kim, S. H., Son, H. J., Park, S. H., Hahn, J. S. & Kim, D. H. A study for degradation of flexible organic photovoltaic modules via damp-heat test: by accessing individual layers of the module. *Sol. Energy Mater. Sol. Cells* **144**, 187–193 (2016).
55. Planes, E. et al. Encapsulation effect on performance and stability of organic solar cells. *Adv. Mater. Interfaces* **7**, 2000293 (2020).
56. Sapkota, S. B., Spies, A., Zimmermann, B., Dürr, I. & Würfel, U. Promising long-term stability of encapsulated ITO-free bulk-heterojunction organic solar cells under different aging conditions. *Sol. Energy Mater. Sol. Cells* **130**, 144–150 (2014).
57. Son, H. J., Kim, S. H. & Kim, D. H. Critical impact of hole transporting layers and back electrode on the stability of flexible organic photovoltaic module. *Adv. Energy Mater.* **7**, 1601289 (2016).
58. Wachsmuth, J. et al. Overcoming moisture-induced degradation in organic solar cells. *Adv. Eng. Mater.* **25**, 2300595 (2023).

## Acknowledgements

We would like to acknowledge the financial support from the National Natural Science Foundation of China grant numbers 22135001 (Q.L.), 22109172 (J.F.) and 22075315 (C.-Q.M.), the Chinese Academy of Sciences Special Research Assistant Program grant number E3551302 (N.W.) and the Chinese Academy of Sciences grant number YJKYYQ20180029 (C.-Q.M.). We are grateful for the technical support from the Suzhou Institute of Nano-Tech and Nano-Bionics for the GIWAXS and TOF-SIMS testing in Nano-X.

## Author contributions

J. Qin, Q.L. and C.-Q.M. conceived the idea and C.-Q.M. and Q.L. supervised the research. J. Qin performed the fabrication and characterization of organic solar cells. C.-Q.M. and J. Qin analysed and established a diffusion model for water vapour. C.-Q.M., J. Qin, Q.X., B.L., N.W. and M.J. analysed the mechanism of the thermal stability of organic solar cells. C.Y. and W.L. synthesized and provided cross-linked fullerene ($PC_{61}PeA$). J.F. and J. Qiu provided assistance in the preparation and certification of high-efficiency organic solar cells. N.W. and W.W. set up the LBIC test equipment and conducted the LBIC test. Zhenguo Wang assisted in the preparation of flexible organic solar cells. Q.Z. conducted GIWAXS test on the active layer. Zhen Wang and Y.D. provided assistance in analysing the two-dimensional diffusion process of water vapour.

## Competing interests

The authors declare no competing interests.

## Additional information

**Supplementary information** The online version contains supplementary material available at https://doi.org/10.1038/s41560-025-01885-8.

**Correspondence and requests for materials** should be addressed to Qun Luo or Chang-Qi Ma.

**Peer review information** *Nature Energy* thanks the anonymous reviewers for their contribution to the peer review of this work.

**Reprints and permissions information** is available at www.nature.com/reprints.

nature research

Corresponding author(s): Changqi Ma

# Solar Cells Reporting Summary

Nature Research wishes to improve the reproducibility of the work that we publish. This form is intended for publication with all accepted papers reporting the characterization of photovoltaic devices and provides structure for consistency and transparency in reporting. Some list items might not apply to an individual manuscript, but all fields must be completed for clarity.

For further information on Nature Research policies, including our data availability policy, see Authors & Referees.

## Experimental design

**Please check: are the following details reported in the manuscript?**

### 1. Dimensions

| | | |
|---|---|---|
| Area of the tested solar cells | ☒ Yes<br>☐ No | The dimensions of the tested solar cells were 2.56mm^2 and 6.25mm^2. |
| Method used to determine the device area | ☒ Yes<br>☐ No | The designated illumination area defined by a thin metal mask of 2.56 mm^2 and 6.25^mm2. |

### 2. Current-voltage characterization

| | | |
|---|---|---|
| Current density-voltage (J-V) plots in both forward and backward direction | ☐ Yes<br>☒ No | No J-V hysteresis observed in these organic solar cells. Current density-voltage (J-V) plots in forward direction. |
| Voltage scan conditions<br>*For instance: scan direction, speed, dwell times* | ☒ Yes<br>☐ No | Cells are measured in forward direction with a step of 0.01V and the dwell time is 0.1 s for every point in our lab. |
| Test environment<br>*For instance: characterization temperature, in air or in glove box* | ☒ Yes<br>☐ No | The J-V characteristics were conducted in glove box at temperature of 25 °C in our lab. The cells for third-party certification were conducted in air at temperature of 25 °C. |
| Protocol for preconditioning of the device before its characterization | ☐ Yes<br>☒ No | No preconditioning of the device before its characterization. |
| Stability of the J-V characteristic<br>*Verified with time evolution of the maximum power point or with the photocurrent at maximum power point; see ref. 7 for details.* | ☒ Yes<br>☐ No | The long-term stability of PM6:BO-4Cl:PC61PeA-based devices under maximum power point (MPP) tracking were performed with continuous illumination in N2-filled chamber, as shown in Supplementary Figure 25. |

### 3. Hysteresis or any other unusual behaviour

| | | |
|---|---|---|
| Description of the unusual behaviour observed during the characterization | ☐ Yes<br>☒ No | No hysteresis or any other unusual behavior was observed during the characterization of organic solar cells. |
| Related experimental data | ☐ Yes<br>☒ No | N/A |

### 4. Efficiency

| | | |
|---|---|---|
| External quantum efficiency (EQE) or incident photons to current efficiency (IPCE) | ☒ Yes<br>☐ No | External Quantum Efficiency (EQE) data for the devices are provided in Supplementary Figure 19 and calculated short-circuit current densities are comparable to that derived from J-V plots. |
| A comparison between the integrated response under the standard reference spectrum and the response measure under the simulator | ☒ Yes<br>☐ No | Integrated EQE under AM1.5 is comparable to current density under solar simulator. |
| For tandem solar cells, the bias illumination and bias voltage used for each subcell | ☐ Yes<br>☒ No | No tandem cells are reported in the work. |

### 5. Calibration

| | | |
|---|---|---|
| Light source and reference cell or sensor used for the characterization | ☒ Yes<br>☐ No | The light source is a solar simulator (Zolix, Sirius-SS150A). |

| | | |
|---|---|---|
| Confirmation that the reference cell was calibrated and certified | ☒ Yes<br>☐ No | The light intensity of solar simulator for J–V measurement was calibrated with a reference silicon cell (QE-B1, Zolix) |
| Calculation of spectral mismatch between the reference cell and the devices under test | ☐ Yes<br>☒ No | Mismatch is not calculated. |

## 6. Mask/aperture

| | | |
|---|---|---|
| Size of the mask/aperture used during testing | ☒ Yes<br>☐ No | Mask area of 2.56 mm^2 and 6.25 mm^2 were used. |
| Variation of the measured short-circuit current density with the mask/aperture area | ☐ Yes<br>☒ No | There is no variation |

## 7. Performance certification

| | | |
|---|---|---|
| Identity of the independent certification laboratory that confirmed the photovoltaic performance | ☒ Yes<br>☐ No | National PV Industry Measurement and Testing Center (Fuzhou, China) |
| A copy of any certificate(s)<br>*Provide in Supplementary Information* | ☒ Yes<br>☐ No | A copy of certificate will be provided in Supplementary Information. |

## 8. Statistics

| | | |
|---|---|---|
| Number of solar cells tested | ☒ Yes<br>☐ No | More than 6 cells for each different types of cells were tested. |
| Statistical analysis of the device performance | ☒ Yes<br>☐ No | We have a statistical analysis of the performance included in the manuscript. Supplementary Table 8 shows the best and average efficiencies with standard deviation. |

## 9. Long-term stability analysis

| | | |
|---|---|---|
| Type of analysis, bias conditions and environmental conditions<br>*For instance: illumination type, temperature, atmosphere humidity, encapsulation method, preconditioning temperature* | ☒ Yes<br>☐ No | Long-term thermal stability testing of various types of batteries was performed using a hot plate heated in a N2 glove box. Damp heat and thermal cycling tests were carried out in an environmental chamber. These samples were only removed from the chamber for J-V scanning and put back immediately after the measurements. |